The lysosomal adaptor JIP3 activates dynein-dynactin via a short coiled coil

Kashish Singh[1#], Clinton K. Lau[1#], José B. Gama[2], Reto Gassmann[2] and Andrew P. Carter[1*]

1. MRC Laboratory of Molecular Biology, Francis Crick Ave, Cambridge, CB2 0QH, UK
2. Instituto de Investigação e Inovação em Saúde-i3S, Universidade do Porto, Porto, Portugal

# Equal Contributions

*Correspondence to cartera@mrc-lmb.cam.ac.uk

Abstract:

Transport of organelles is critical for maintaining healthy neurons. A key adaptor for moving lysosomes in axons is JIP3, which binds both kinesin and dynein motors. Unlike many known dynein adaptors JIP3 contains only a short coiled coil, raising the question of whether, like them, it can activate long distance transport. Here we show a short construct of JIP3 containing residues 1-185 is sufficient to stimulate long distance movement of dynein-dynactin *in vitro*. Using cryoEM to solve the structure of the resulting complexes on microtubules we describe how one copy of JIP3 recruits two dyneins to dynactin. The data show that even short adaptors lacking an interaction with dynactin's pointed end are sufficient to activate motility.

Introduction:

In neuronal axons there is a continuous bidirectional movement of organelles driven by microtubule motors. This transport plays key roles in supplying synapses, clearing unwanted or damaged components and mediating retrograde signaling back to the cell body (Guedes-Dias and Holzbaur 2019). JIP3 (c-Jun-N-terminal kinase-interacting protein 3) is emerging as an important adaptor linking motors to axonal organelles. Originally identified as a scaffolding protein which activates JNK kinase (Ito et al. 1999, Kelkar et al. 2000), JIP3 and its homologs (Sunday Driver in *D. melanogaster* and UNC-16 in *C. elegans*) were subsequently identified as binding the plus-end/anterograde motor kinesin-1 (Bowman et al. 2000, Verhey et al. 2001), the minus-end/retrograde motor dynein (Arimoto et al. 2011) and the dynein co-factor dynactin (Cavalli et al. 2005, Montagnac et al. 2009).

There is some evidence for a role for JIP3 in anterograde/kinesin-driven movement of TrkB containing vesicles (Huang et al. 2011) and the protein JIP1 (Hammond et al. 2008). However, the main defect from loss of JIP3 function is the large accumulation of organelles in the axon (Bowman et al. 2000, Byrd et al. 2001, Drerup and Nechiporuk 2013, Edwards et al. 2013, Gowrishankar et al. 2017, Gowrishankar et al. 2021) suggesting defects in clearance. Studies in zebrafish and mice show specific defects in retrograde transport of lysosomes, but not mitochondria, in the absence of JIP3 (Drerup and Nechiporuk 2013, Gowrishankar et al. 2017). Furthermore, labelled JIP3 moves retrogradely with autophagosomes and its knockdown reduces their motility (Cason et al. 2021). Taken together these observations suggest a major role of JIP3 is as an adaptor linking lysosomes to the retrograde motor dynein.

A large family of adaptors are known which recruit dynein-dynactin to cellular cargoes and activate the motor's long-range movement (Reck-Peterson et al. 2018). A common feature of these activating adaptors is the presence of a >200 amino acid long coiled coil that spans the length of the dynactin filament (Urnavicius et al. 2015, Urnavicius et al. 2018). The N-terminal end contains, or is linked to, a binding site for the dynein light intermediate chain (DLIC) C-terminal helix. Different subfamilies use different domains for this purpose including the CC1 box motif, hook domain, EF-hands and RUN domain (Schroeder et al. 2014, Schroeder and Vale 2016, Gama et al. 2017, Lee et al. 2018, Reck-Peterson et al. 2018, Lee et al. 2020, Keren-Kaplan et al. 2022, Kumar et al. 2022). The C-terminal end of the coiled coil contacts the dynactin pointed end complex (Urnavicius et al. 2015). A conserved Spindly-box motif (Gama et al. 2017), frequently separated from the coiled-coil by a loop (Chaaban and Carter 2022, d'Amico et al. 2022), plays a key role in this interaction (Lau et al. 2021, Chaaban and

Carter 2022). Further, a dynein heavy chain binding site motif (HBS1 or previously the CC2 box) is present between the DLIC binding site and the Spindly box (Sacristan et al. 2018, Chaaban and Carter 2022).

JIP3, its paralog JIP4 and the related RILP proteins (RILP, RILPL1 and RILPL2) share a similar architecture (Vilela et al. 2019). At their N-termini is an RH1 (RILP Homology 1) domain which, with the exception of RILPL2, binds the DLIC C-terminus (Celestino et al. 2022). Like other dynein adaptors, the RH1 domain is followed by a stretch of coiled coil, but unlike other adaptors this region is too short to span the length of dynactin (Reck-Peterson et al. 2018). This raises the question of whether JIP3 and its relatives are able to activate dynein movement and how they bind to the dynein-dynactin complex.

To address this, we show that the JIP3 RH1 domain and its adjacent coiled coil are sufficient to activate dynein-dynactin complexes. We then use cryoEM to solve the structure of dynein-dynactin-JIP3 on microtubules which shows that JIP3 recruits and interacts with two dyneins. Further, unlike other dynein adaptors, JIP3 does not seem to require interactions with the dynactin pointed end to activate motility.

Results

JIP3$_{1-185}$ activates dynein movement *in vitro*

Full length JIP3 contains an N-terminal RH1 domain and coiled coil called LZI (Leucine Zipper I). This is followed by a disordered region, two subsequent coiled coils (LZII and RH2) and a large C-terminus containing a WD40 domain (Vilela et al. 2019) (Figure 1A). Initially we expressed and purified full length JIP3, however, were unable to observe any activation of dynein motility *in vitro* (data not shown). As other full-length dynein adaptors are known to be autoinhibited (Hoogenraad et al. 2003, d'Amico et al. 2022) we generated a JIP3 truncation (1-185) consisting of just the RH1 domain and LZI coiled coil (Celestino et al. 2022). We performed pull down experiments from pig brain lysates and immunoblotted for the p150^{Glued} component of dynactin and the dynein intermediate chain (DIC) (Figure 1B). The data suggest JIP3$_{1-185}$ specifically pulls down both dynein and dynactin with a similar efficiency as a fragment of the known activating adaptor BICD2 (BICD$_{22-422}$).

To directly assay for activation, we performed *in vitro* motility assays using microtubules immobilized on coverslips in the presence of recombinant TMR-labelled human dynein and pig-brain dynactin (Schlager et al. 2014). We added recombinant human Lis1, which has recently been shown to increase the robustness of dynein activation (Elshenawy et al. 2020, Htet et al. 2020). We observed few processive movements of TMR-dynein (defined as a continuous movement of more than 5 pixels – 525nm) when only dynactin and Lis1 are present (no adaptor). In contrast addition of JIP3$_{1-185}$ resulted in multiple long distance runs of TMR-dynein (Figure 1C, D). The mean frequency over three independent experiments was 1.15 ±0.45 (SD) events/µm microtubule/min, which is very similar to that of the dynein adaptor HOOK3 collected under equivalent experimental conditions (Garner et al. 2022). The mean velocity of the complexes was 1.00 ±0.2 µm/s (Figure 1E) which is also comparable to the velocity of HOOK3 complexes (Garner et al. 2022). Under the conditions used in our assays we determined a run length for JIP3 complexes of 3.8 µm (Figure 1F). Collectively these data show that a minimal JIP3$_{1-185}$ construct is able to activate dynein's long-range movement *in vitro* in the presence of dynactin.

JIP3 recruits two dyneins per dynactin

The short length of JIP3's LZI in comparison to N-terminal coiled coils of other dynein adaptors (Figure 1A) raises the question of how it activates dynein. To directly address this, we mixed dynein, dynactin and JIP3$_{1-185}$ with microtubules in the presence of the non-hydrolysable nucleotide analog AMPPNP and applied this mixture to cryo-EM grids before vitrification. Cryo-EM images revealed dynein-dynactin complexes bound to microtubules (Figure 2A). These were similar in appearance to those observed previously with the adaptor BICDR1 (Chaaban and Carter 2022), suggesting, as expected, that JIP3 activates dynein via its recruitment to dynactin.

To determine the structure of these complexes we modified published protocols (Chaaban and Carter

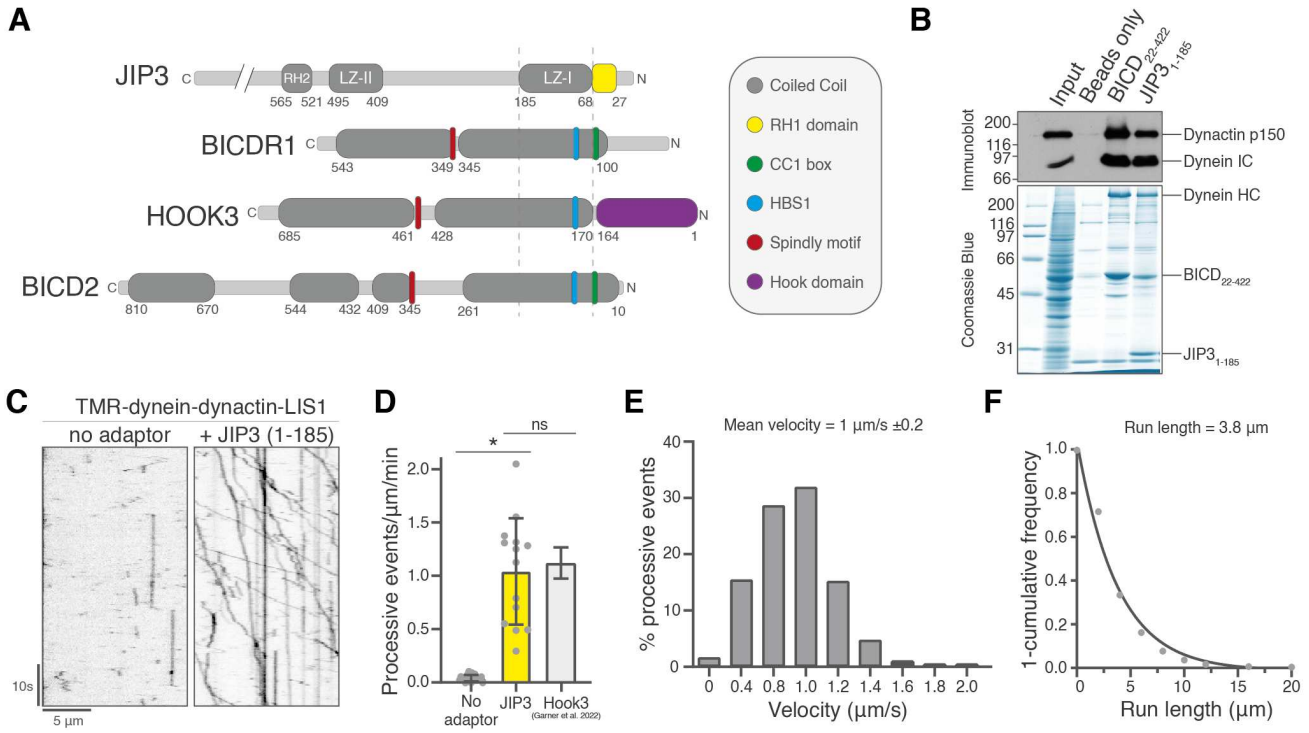

Figure 1. JIP3 is an activating adaptor for dynein motility *in vitro*. (A) Schematic representation of JIP3, BICDR1 (also known as BICDL1), HOOK3 and BICD2. The dotted lines are shown to illustrate the short coiled coil of JIP3 as compared to some of the known dynein activating adaptors. **(B)** Immunoblot of pig brain lysate pull down using antibodies against dynactin p150 and dynein intermediate chain (top) and its corresponding Coomassie Blue stained SDS PAGE gel (bottom). Molecular weight is in kDa. **(C)** Kymographs of TMR-dynein-dynactin-LIS1 in the absence (left) and presence of $JIP3_{1-185}$. Experiments were performed in triplicates. **(D)** The number of processive events per µm microtubule per minute was determined in three technical replicates, with the mean ±S.D. plotted. The total number of movements analyzed were 767 for JIP3, and 52 for the no adaptor control. Significance was determined using ANOVA with Tukey's multiple comparison (ns = not significant, * = p≤0.05). The data for HOOK3 (Garner et al. 2022) was used for comparison. **(E)** Distribution of velocities from 767 processive events for dynein-dynactin-$JIP3_{1-185}$ along with mean velocity ±S.D. (n=3). **(F)** A one-cumulative frequency distribution plot showing run-length for dynein-dynactin-$JIP3_{1-185}$, with fit to a one-phase exponential decay. The decay constant (run length) is shown.

2022, Chai et al. 2022) to rapidly subtract the microtubules from the raw micrographs. This aids particle picking and allows subsequent refinement steps to focus on the dynein-dynactin complexes. In summary (Figure 2A and S1) we implemented crYOLO (Wagner et al. 2019) to pick individual particles along the microtubules and then used the identified positions for subtraction of the microtubules as described (Chai et al. 2022). We then used cryoSPARC (Punjani et al. 2017) for ab-initio model generation and for initial particle sorting via heterogeneous refinement. Finally, signal subtraction, 3D classifications and focused refinements were performed in RELION (Zivanov et al. 2018) as previously described (Chaaban and Carter 2022). These optimized steps allowed us to subtract microtubules from the raw micrographs and achieve an initial reconstruction of the dynein-dynactin-JIP3 complex within three days.

The initial reconstruction showed clear density for dynactin, dynein tails and JIP3. The dynein motor domains were at a lower resolution due to their flexible position. The reconstruction shows that $JIP3_{1-185}$ recruits two dynein dimers (dynein-A and dynein-B) per dynactin (Figure 2B). The dynein tails lie next to each other, with their heavy chains (A1, A2, B1 and B2) sitting in the grooves formed along the dynactin filament, as described for other adaptors (Urnavicius et al. 2015, Urnavicius et al. 2018). Unlike our recent BICDR1 structure, which had two copies of the adaptor bound, this work shows only a single copy of $JIP3_{1-185}$. This $JIP3_{1-185}$ runs along the cleft between the dyneins and dynactin in a similar position to other adaptors. The

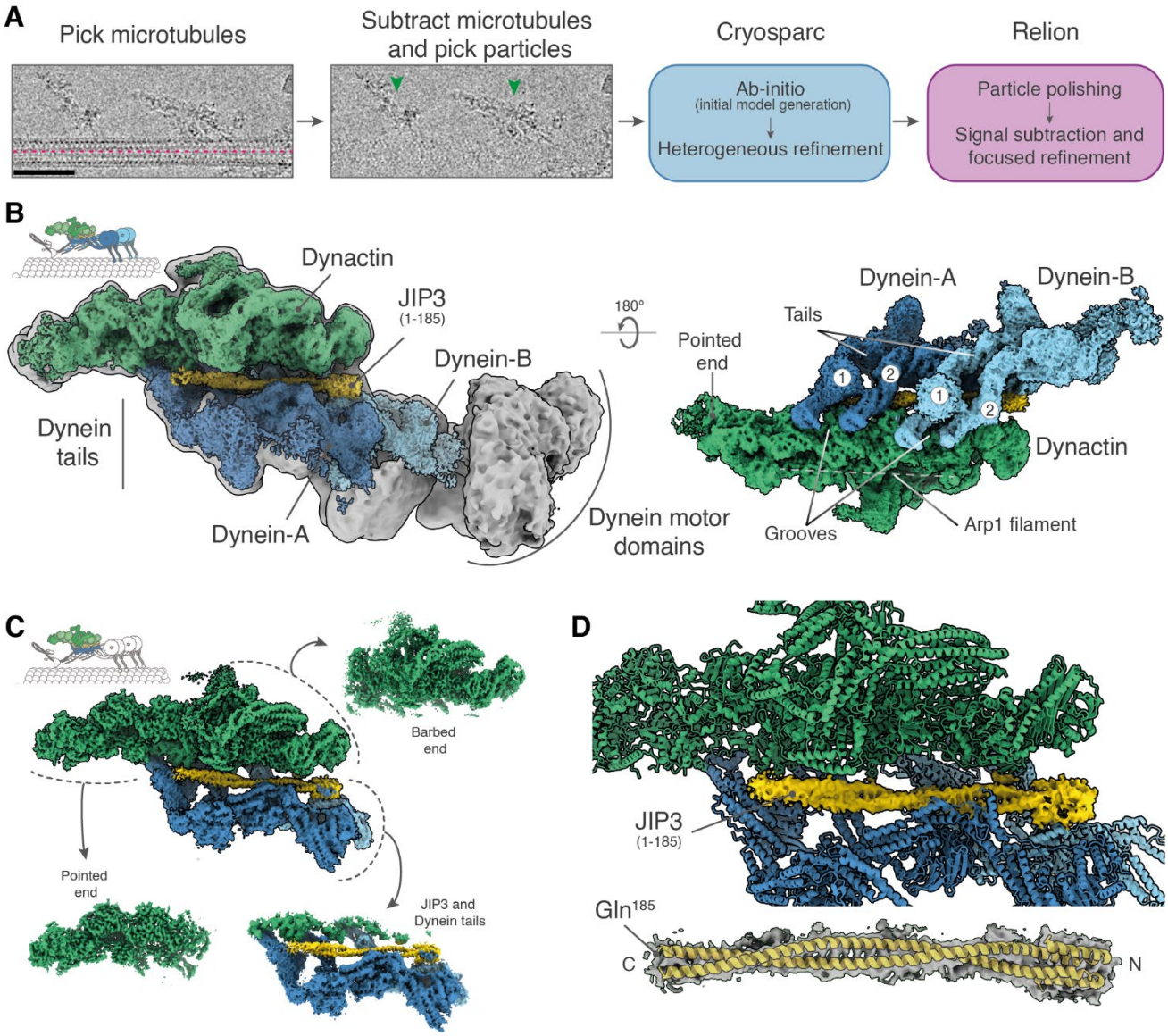

Figure 2. Cryo-EM structure of dynein-dynactin-JIP3 on microtubules. (A) Overview of the processing pipeline used to go from raw micrographs to 3D reconstruction. Scale bar: 50 nm. **(B)** Consensus structure showing the different components of the complex: dynactin (green), dynein (blue) and JIP3 (yellow). In grey is the consensus structure low pass filtered to 25 Å to show the flexible dynein motor domain. JIP3 recruits two dynein molecules to dynactin. **(C)** Composite density map of dynein-dynactin-JIP3 along with the locally refined regions of the complex used to generate the composite. **(D)** The cryoEM density for JIP3 in the structure accounts for the full $JIP3_{1-185}$ as shown by the AlphaFold prediction of $JIP3_{1-185}$ modelled into the density.

most striking feature, however, is that the $JIP3_{1-185}$ density ends after contacting the dynein tails without extending to contact the dynactin pointed end.

To understand the connections $JIP3_{1-185}$ makes we performed focused refinement of three separate parts of the structure to generate a higher resolution composite map of the complex (Figure 2C). The improved density shows that the JIP3 construct consists of a 20nm long coiled coil, ending in the four helical bundle RH1 domain (Vilela et al. 2019). An AlphaFold model of the $JIP3_{1-185}$ construct fits the density with no extra residues at the C-terminal end (Figure 2D). Therefore, the density we see for JIP3 accounts for the entire length of the coiled coil in the construct we used. This shows that the interactions observed in our structure are sufficient to account for its ability to activate dynein movement.

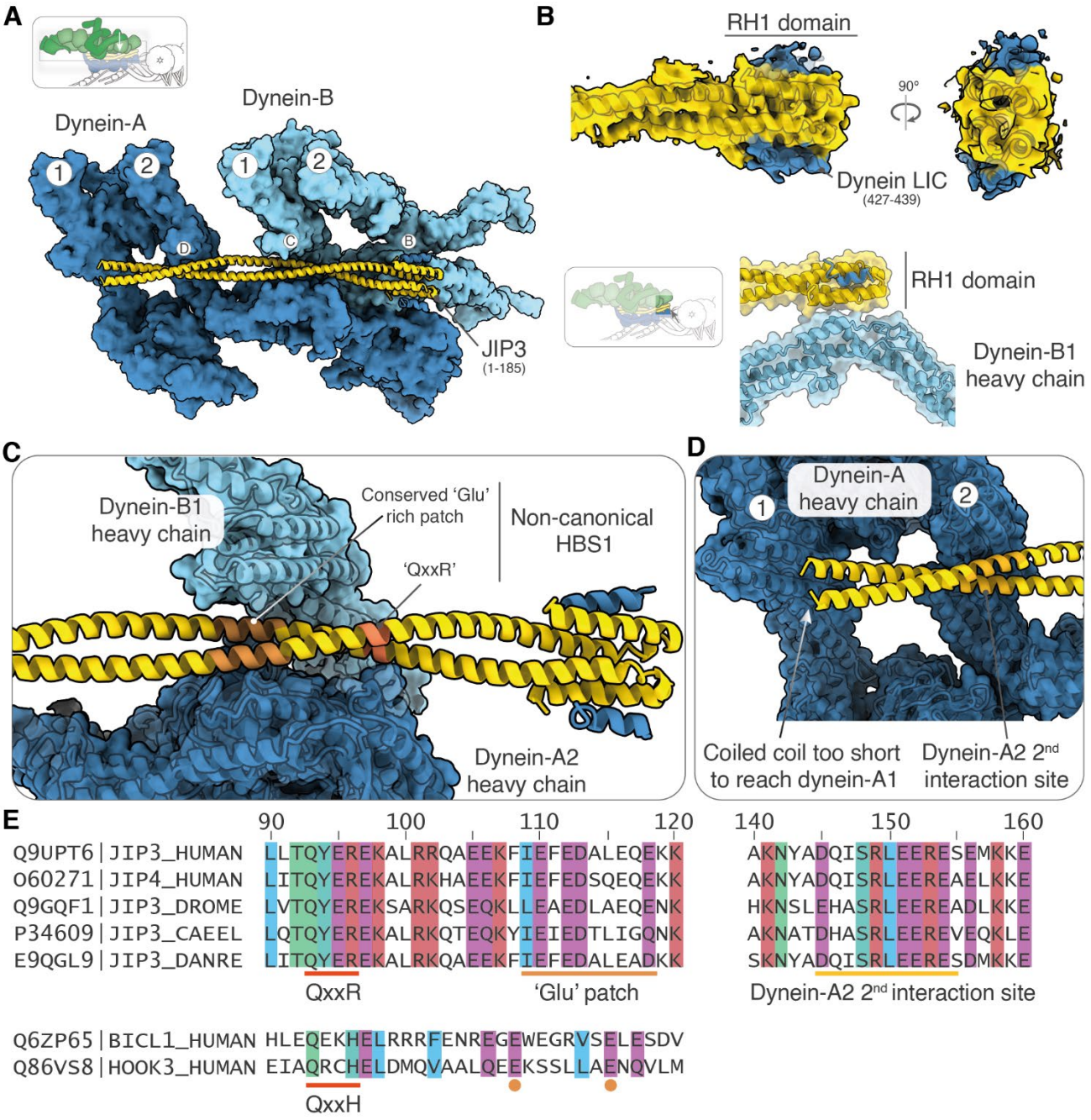

Figure 3. JIP3 interactions with dynein. **(A)** Trajectory of JIP3 along the dynein heavy chain tails is shown using a top view of the complex. Dynactin segments are removed to aid visualization. JIP3 binds to both dynein molecules via a total of three interaction sites. **(B)** The N-terminal RH1 domain (yellow) has extra density on either side which is explained by the DLIC C-terminal helix (blue). The AlphaFold prediction of this interaction is displayed as cartoon inside the density. The RH1 domain is docked against the dynein-B1 heavy chain. **(C)** JIP3 interacts with dynein heavy chains using a non-canonical HBS1 sequence QxxR and a conserved glutamate patch. Here the JIP3 is sandwiched between helical-bundle 2 of dynein-B1 and helical-bundle 5 of dynein-A2. **(D)** JIP3 interaction with the helical-bundle 2 of dynein-A2. **(E)** Sequence alignment of the JIP3 HBS1 region and the dynein-A2 2nd interaction site (top). The residues involved in interactions with dynein are highly conserved. Sequences of canonical HBS1 from BICDR1 and HOOK3 are shown for comparison (bottom). The Uniprot codes are indicated on the left.

Interactions between JIP3$_{1\text{-}185}$ and dynein-dynactin

Our density suggests JIP3$_{1\text{-}185}$ does not make any tight connections to dynactin. Instead its three main sites of interaction all involve the dynein tails (Figure 3A). The JIP3 N-terminal RH1 domain shows extra density (Figure 3B) consistent with the presence of DLIC C-terminal helices (Celestino et al. 2022). Notably both sides of the RH1 domain are occupied suggesting two DLIC C-termini are bound.

Geometric constraints make it most likely that one of these comes from dynein-A and the other from dynein-B. The RH1 domain is visible in our density in part because it also docks against the dynein-B1 heavy chain (Figure 3B – lower panel and S2).

The second major interaction site involves the region of JIP3 between residues 90 and 120 which is sandwiched between the dynein-A2 and B1 heavy chains (Figure 3C, 3E). This part of JIP3 contains conserved residues which resemble the previously described HBS1 (Heavy chain Binding Site 1) (Sacristan et al. 2018, Chaaban and Carter 2022). The HBS1 in BICDR1 and HOOK adaptors contains a QxxY/H followed by a patch of conserved glutamates. In JIP3 the equivalent motif is QxxR and the spacing to the glutamate (Glu) patch is slightly different (Figure 3E). The JIP3 HBS1 interacts with the same region of dynein-A2 as the that of BICDR1 (Chaaban and Carter 2022). This is helical-bundle 5 of the dynein heavy chain (Urnavicius et al. 2018), around residue Tyr827. However, consistent with the differences in sequence, the interactions differ slightly with the Gln94 of the QxxR motif sitting on the opposite side of dynein Tyr827 compared to the equivalent Gln150 residue in BICDR1. The Glu patch interacts with both the helical-bundle5 region of dynein-A2 on one side of JIP3 and the helical-bundle 2 region of dynein-B1 on the other.

The third interaction involves residues between 145 and 155 on JIP3 (Figure 3D). This also contacts dynein-A2, but via its helical-bundle 2 region. This combination of interactions with the two sites on dynein-A2 is common to other dynein adaptors (Urnavicius et al. 2018). The coiled coil of JIP3 approaches the helical bundle2 region of dynein-A1, but is too short to directly contact it.

Discussion

The work presented here shows that JIP3 can activate dynein-dynactin complex formation and long-range dynein movement *in vitro*, despite a much smaller coiled coil than other dynein cargo adaptors. JIP3 is part of a family of RH1 domain-containing proteins (Wang et al. 2004, Vilela et al. 2019) raising the question of whether they will also work in a similar way. The closest homolog is JIP4, which is also associated with lysosome movement, both in neurons (Gowrishankar et al. 2021) and non-neuronal cells (Willett et al. 2017). Given the sequence alignment with JIP3 throughout the dynein-dynactin binding region it seems likely this adaptor binds similarly to JIP3.

More distant relatives include RILP, RILPL1 and RILPL2. RILP directly binds to the small GTPase Rab7 (Wu et al. 2005), recruits dynein/dynactin to late endosomes and lysosomes (Jordens et al. 2001) and interacts with the DLIC C-terminus (Schroeder et al. 2014, Celestino et al. 2022). Unlike JIP3, we have not yet been able to detect dynein activation with RILP, but this may be due to not yet finding a construct in which autoinhibition mechanisms are removed. AlphaFold predicts the coiled coil after the RH1 domain is interrupted by two short loops, but otherwise has a similar length to the $JIP3_{1\text{-}185}$ construct. Overall, it seems likely that RILP can activate dynein-dynactin complex formation. A chimeric RILPL1 containing RILPs Rab7 binding region can cluster lysosomes at the center of the cell suggesting it is able to recruit dynein (Wang et al. 2004). RILPL1 has also been shown to interact with the DLIC C-terminus *in vitro* (Celestino et al. 2022) further indicating that it could also be a dynein adaptor. No evidence has linked RILPL2 to dynein, whereas it has been shown to be linked to the actin motor Myosin-Va (Lise et al. 2009).

Our dynein-dynactin-JIP3 structure shows that an interaction with the dynactin pointed-end complex is not required for activation of dynein *in vitro*. Another surprise from this work is that there appear to be few, if any, interactions between JIP3 and the dynactin complex along the length of the adaptor. This suggests that the role of $JIP3_{1\text{-}185}$ is to orient and stabilize the binding of two dyneins to each other so that their heavy chain tails can interact with the grooves along the dynactin filament.

One question that arises is what role the pointed-end interactions play in other adaptors given our observations that they are not required to recruit dynein to dynactin. The most obvious possibility is that they add stability to the complex, which, in the case of JIP3 could be offset by an intrinsically higher affinity for dynein. Another possibility is that a role of the pointed-end interactions is particularly important for those adaptors which bind to dynein-dynactin in pairs. In our recent structures of BICDR1 and HOOK3 complexes, it is clear that the two

different copies of the adaptor are offset with respect to each other and that this comes in part from the different interactions each makes with the pointed end complex (Chaaban and Carter 2022).

A key motif driving interaction with the dynactin pointed end in many dynein adaptors is the Spindly-box consisting of LϕXEϕ, where ϕ denotes a hydrophobic side chain (Gama et al. 2017). This forms a helix that binds to a site on the pointed-end component p25 (Lau et al. 2021, Chaaban and Carter 2022). There often appears to be a region of disorder between the end of the adaptor coiled coil and the Spindly motif. A canonical Spindly motif is not apparent in JIP3 or other RH1 family adaptors (Celestino et al. 2022, Chaaban and Carter 2022). This may reflect the lack of requirement of a pointed end interaction for activation, or the possibility that a non-canonical motif is present but has not yet been identified.

Mutations that block the binding of DLIC to JIP3 lead to accumulation of lysosomes at the axon tip, showing JIP3 also recruits kinesin-1 motors in cells (Celestino et al. 2022). JIP3 interacts with both the C-terminus of the kinesin-1 heavy chain, via its RH1 domain (Sun et al. 2011, Celestino et al. 2022) and with the kinesin light chain, via its LZII coiled coil (Nguyen et al. 2005, Watt et al. 2015, Cockburn et al. 2018). DLIC and kinesin can bind simultaneously to the RH1 domain (Celestino et al. 2022) suggesting both motors can bind to JIP3 at the same time. In our structure there is sufficient space around the RH1 domain to accommodate the disordered kinesin C-terminal tail. The dual binding of kinesin and dynein is similar to observations for other activating adaptors such as HOOK3 (Kendrick et al. 2019, Siddiqui et al. 2019) and TRAK1/2 (Fenton et al. 2021, Canty et al. 2022). A key future question is to determine whether this is true and work out how the kinesin and dynein/dynactin are arranged to produce either plus or minus end directed movement along microtubules.

Acknowledgements

We thank S. Chaaban for discussions, assistance in processing microtubule bound dynein/dynactin complexes and AlphaFold modelling. We thank the MRC Laboratory of Molecular Biology Electron Microscopy Facility for access and support of electron microscopy sample preparation and data collection; J. Grimmett and T. Darling for providing scientific computing resources. This work was supported by Wellcome [210711/Z/18/Z], the Medical Research Council, as part of United Kingdom Research and Innovation (also known as UK Research and Innovation) [MRC file reference number MC_UP_A025_1011], and the EMBO Postdoctoral Fellowship [ALTF 197-2021] to K.S.

Competing Interest

The authors declare no competing interests.

Data Availability

Atomic coordinates and cryo-EM maps for the composite dynein tail-dynactin-JIP3 structure, dynactin pointed end, dynactin barbed end and dynein tail-JIP3 regions are available on request (A.P.C) and will be deposited in the Protein Data Bank (PDB) / Electron Microscopy Data Bank (EMDB).

Methods:

Protein expression and purification

Dynactin was purified from frozen porcine brains as previously described (Urnavicius et al. 2015). Fresh brains were cleaned in homogenization buffer (35 mM PIPES pH 7.2, 5 mM $MgSO_4$, 100 µM EGTA, 50 µM EDTA), and flash frozen in liquid nitrogen. Frozen brains were broken into pieces using a hammer. The brain pieces were blended and resuspended in homogenization buffer supplemented with 1.6 mM PMSF, 1 mM DTT, and 4 complete-EDTA protease-inhibitor tablets per 500 mL (Roche). After thawing, the lysate was centrifuged in a JLA 16.250 rotor (Beckman Coulter) at 16,000 rpm for 15 min at 4°C. The supernatant was further clarified in a Type 45 Ti rotor (Beckman Coulter) at 45,000 rpm for 50 min at 4°C. After filtering the supernatant in a Glass Fibre filter (Sartorius) and a 0.45 µm filter (Elkay Labs), it was loaded on a column packed with 250 mL of SP-Sepharose (Cytiva) pre-equilibrated with SP buffer

(35 mM PIPES pH 7.2, 5 mM $MgSO_4$, 1 mM EGTA, 0.5 mM EDTA, 1 mM DTT, 0.1 mM ATP) using an Akta Pure system (Cytiva). The column was washed with SP buffer with 3 mM KCl before being eluted in a linear gradient up to 250 mM KCl over 3 column volumes. The peak around ~15 mS/cm was collected and filtered in a 0.22 µm filter (Elkay Labs) before being loaded on a MonoQ 16/10 column (Cytiva) pre-equilibrated with MonoQ buffer (35 mM PIPES pH 7.2, 5 mM $MgSO_4$, 100 µM EGTA, 50 µM EDTA, 1 mM DTT). The column was washed with MonoQ buffer before being eluted in a linear gradient up to 150 mM KCl over 1 column volume, followed by another linear gradient up to 350 mM KCl over 10 column volumes. The peak around ~39 mS/cm was pooled and concentrated to ~3 mg/mL before being loaded on a TSKgel G4000SWXL column (Tosoh Bioscience) preequilibrated with GF150 buffer (25 mM HEPES pH 7.2, 150 mM KCl, 1 mM MgCl2) supplemented with 5 mM DTT and 0.1 mM ATP. The peak at ~114 mL was pooled and concentrated to ~3 mg/mL. 3 µL aliquots were flash frozen in liquid nitrogen and stored at -80°C.

Full length human cytoplasmic dynein-1 (Schlager et al. 2014) and human LIS1 (Baumbach et al. 2017) with N-terminal ZZ-TEV tag were expressed using the Sf9/baculovirus system and purified as previously described (Schlager et al. 2014, Baumbach et al. 2017). Specifically, for cryoEM we used the dynein construct with mutations in the linker (R1567E and K1610E) to help overcome the autoinhibited conformation (Zhang et al., 2017). Fresh bacmid DNA was transfected into Sf9 cells at $0.5x10^6$ cells/mL in 6-well cell culture plates using FuGene HD (Promega) according to the manufacturer's protocol (final concentration 10 µg/mL). After six days, 1 mL of the culture supernatant was added to 50 mL of $1x10^6$ cells/mL and cells were infected for five days in a shaking incubator at 27°C. The P2 virus was isolated by collecting the supernatant after centrifugation at 4,000 rcf for 15 min and stored at 4°C. For expression, 10 mL of P2 virus was used to infect 1 L of Sf9 cells at $1.5\text{-}2x10^6$ cells/mL for 72 hours in a shaking incubator at 27°C. Cells were harvested by centrifugation at 4,000 rcf for 10 min at 4°C, and washed with cold PBS. The cell pellet was flash frozen and stored at -80°C.

For dynein purification, a cell pellet from 1 L expression was resuspended in 50 mL lysis buffer (50 mM HEPES pH 7.4, 100 mM NaCl, 10% (v/v) glycerol, 0.1 mM ATP) supplemented with 2 mM PMSF, 1 mM DTT, and 1 complete-EDTA protease-inhibitor tablet. Cells were lysed using a 40 mL dounce tissue grinder (Wheaton) with ~20 strokes. The lysate was clarified at 503,000 rcf for 45 min at 4°C using a Type 70 Ti Rotor (Beckman Coulter). The supernatant was incubated with 3 mL IgG Sepharose 6 Fast Flow beads (Cytiva) pre-equilibrated with lysis buffer for 4 hours at 4°C. The beads were then applied to a gravity flow column and washed with 150 mL of lysis buffer and 150 mL of TEV buffer (50 mM Tris-HCl pH 7.4, 150 mM KAc, 2 mM MgAc, 1 mM EGTA, 10% (v/v) glycerol, 0.1 mM ATP, 1 mM DTT). For TMR labelled dynein, beads were transferred to a tube and incubated with 10 µM SNAP-Cell TMR-Star dye (New England Biolabs) for 1 h at 4°C prior to the TEV buffer washing step. The beads were then transferred to a 5 mL centrifuge tube (Eppendorf) and filled up completely with TEV buffer. 400 µg TEV protease was added to the beads followed by overnight incubation at 4°C. The beads were transferred to a gravity flow column and the flow through containing the cleaved protein was collected. The protein was concentrated to ~2 mg/mL and loaded onto a TSKgel $G4000_{SWXL}$ column pre-equilibrated with GF150 buffer supplemented with 5 mM DTT and 0.1 mM ATP. Peak fractions were pooled and concentrated to ~2.5-3 mg/mL. Glycerol was added to a final concentration of 10% from an 80% stock made in GF150 buffer. 3 µL aliquots were flash frozen and stored at -80°C.

For LIS1 purification, a cell pellet from 1 L expression was resuspended in 50 mL lysis buffer B (50 mM Tris-HCl pH 8, 250 mM KAc, 2 mM MgAc, 1 mM EGTA, 10% (v/v) glycerol, 0.1 mM ATP, 1 mM DTT) supplemented with 2 mM PMSF. Cells were lysed using a 40 mL dounce tissue grinder (Wheaton) with ~20 strokes. The lysate was clarified at 150,000 rcf for 30 min at 4°C using a Type 45 Ti Rotor (Beckman Coulter). The supernatant was incubated with 3 mL IgG Sepharose 6 Fast Flow

beads (Cytiva) pre-equilibrated with lysis buffer B for 4 hours at 4°C. The beads were then applied to a gravity flow column and washed with 150 mL of lysis buffer B. The beads were then transferred to a 5 mL centrifuge tube (Eppendorf) and filled up completely with lysis buffer B. 400 µg TEV protease was added to the beads followed by overnight incubation at 4°C. The beads were transferred to a gravity flow column and the flow through containing the cleaved protein was collected. The protein was concentrated to ~5 mg/mL and loaded onto a Superdex 200 Increase 10/300 (Cytiva) column pre-equilibrated with GF150 buffer supplemented with 5 mM DTT and 0.1 mM ATP. Peak fractions were pooled and concentrated to ~5 mg/mL. Glycerol was added to a final concentration of 10% from an 80% stock made in GF150 buffer. 5 µL aliquots were flash frozen and stored at -80°C.

$JIP3_{1-185}$ construct (Celestino et al. 2022) was expressed and purified as previously described (Celestino et al. 2022). Briefly, the protein fragment from mouse cDNA was inserted into a 2CT vector [N-terminal 6xHis::maltose binding protein (MBP) followed by a TEV protease cleavage site and C-terminal Strep-tag II]. It is important to note that the mouse $JIP3_{1-185}$ sequence is identical to human JIP3. The protein was expressed in SoluBL21 *E. coli* strain where the expression was induced overnight at 18°C with 0.1mM IPTG added at O.D of 0.6-0.8. Cells were harvested by centrifugation at 4,000 rcf for 20 min followed by a PBS wash and another centrifugation at 4,000 rcf for 20 min. The cell pellet was flash frozen in liquid nitrogen and stored at -80°C. Pellet from a 2L culture was resuspended in 50ml lysis buffer C (50 mM HEPES pH 8.0, 250 mM NaCl, 10 mM imidazole, 0.1% Tween20, 1 mM DTT, 1 mM PMSF, 2 mM benzamidine-HCl) supplemented with 1 complete-EDTA protease-inhibitor tablet and 1mg/mL Lysozyme. Cells were lysed by sonication and the lysate was clarified at 150,000 rcf for 30 min at 4°C using a Type 45 Ti Rotor (Beckman Coulter). The lysate was passed though 2ml of pre-equilibrated Ni-NTA Agarose beads (Qiagen) in a gravity flow column, three times and then washed with 300ml of wash buffer (25 mM HEPES pH 8.0, 250 mM NaCl, 25 mM imidazole, 0.1% Tween20, 1 mM DTT, 1 mM PMSF, 2 mM benzamidine-HCl). Proteins were eluted elution buffer A (50 mM HEPES pH 8.0, 150 mM NaCl, 250 mM imidazole, 1 mM DTT, 2 mM benzamidine-Cl). Fractions containing the protein were pooled, incubated overnight at 4°C with TEV protease and then incubated in batch with Strep-Tactin Sepharose resin (IBA) for 1 h at 4°C, and washed with wash buffer B (25 mM HEPES pH 8.0, 250 mM NaCl, 0.1 % Tween 20, 1 mM DTT). Proteins were eluted on a gravity column with elution buffer B (50 mM HEPES pH 7.5, 150 mM NaCl, 3.5 mM desthiobiotin). The protein was further purified by size exclusion chromatography on a Superose 6 Increase 10/300 column (Cytiva) equilibrated with storage buffer (25 mM HEPES pH 7.5, 150 mM NaCl, 1mM MgCl2, 1mM DTT). Glycerol was added to a final concentration of 10% (v/v) and aliquots were flash frozen in liquid nitrogen and stored at -80°C.

Pull down from brain lysate

50 pmol of purified recombinant BICD2(2-422)::Strep-tag II or JIP3(1-185)::Strep-tag II were added to 15 µL (bed volume) of Strep-Tactin Sepharose resin (IBA Lifesciences) in 100 µL pull-down buffer (30 mM HEPES pH 7.4, 50 mM K-acetate, 2 mM Mg-acetate, 5 mM DTT, 1 mM EGTA, 10 % (v/v) glycerol, 0.1 % (v/v) IGEPAL), and mixtures were incubated with rotation at 4 °C for 30 min. 100 µL of cleared porcine brain lysate, prepared as described (McKenney et al. 2014) and containing fresh 1 mM PMSF, and 300 µL of pull-down buffer were added to the proteins pre-bound to resin, and mixtures were incubated for another hour. The resin was washed with 3 × 500 µL of pull-down buffer, and proteins were eluted for 15 min at room temperature with 50 µL of elution buffer (100 mM Tris-HCl pH 8.0, 150 mM NaCl, 1 mM EDTA, 10 mM desthiobiotin). For SDS-PAGE, 12 µL of 4x SDS-PAGE sample buffer were added to 36 µL of the eluted fractions, and 10 µL were loaded per lane. Immunoblotting was carried out as described (Celestino et al. 2022). Membranes were co-incubated with mouse monoclonal antibodies against dynactin p150 (BD Transduction Laboratories 610473, 1:2500) and dynein intermediate chain 70.1 (Sigma D5167, 1:2500), followed by incubation with goat polyclonal anti-mouse IgG/IgM antibodies coupled to HRP (Jackson

ImmunoResearch 115-035-044, 1:10000). Proteins were visualized by chemiluminescence using ECL substrate (Pierce) and X-ray film (Amersham).

In vitro TIRF motility assays

In vitro TIRF assays were carried out as previously described (Urnavicius et al. 2018). Microtubules were prepared the day before the assay was performed. Microtubules were made by mixing 1 µL of 2 mg/mL HiLyte Fluor 488 tubulin (Cytoskeleton), 2 µL of 2 mg/mL, biotinylated tubulin (Cytoskeleton) and 7 µL of 6 mg/mL unlabelled pig tubulin (Schlager et al. 2014) in BRB80 buffer (80 mM PIPES pH 6.8, 1 mM MgCl2, 1 mM EGTA, 1 mM DTT). 10 µL of polymerization buffer (2× BRB80 buffer, 20% (v/v) DMSO, 2 mM Mg.GTP) was added followed by incubation at 4°C for 5 min. Microtubules were polymerized at 37°C for 1 h. The sample was diluted with 100 µL of MT buffer (BRB80 supplemented with 40 µM paclitaxel), then centrifuged on a benchtop centrifuge (Eppendorf) at 21,000 rcf for 9 minutes at room temperature. The resulting pellet was gently resuspended in 100 µL of MT buffer, then centrifuged again as above. 50 µL MT buffer was then added and the microtubule solution was protected from light. Before usage, and every 5 hours during data collection, the microtubule solution was spun again at 21,000 rcf for 9 minutes, and the pellet resuspended in the equivalent amount of MT buffer.

Motility chambers were prepared by applying two strips of double-sided tape approximately 8-10nm apart on a glass slide and then placing a piranha-solution-cleaned coverslip on top. The coverslip was functionalized using PLL-PEG-Biotin (SuSOS AG), washed with 50 µL of TIRF buffer (30 mM HEPES pH 7.2, 5 MgSO4, 1 mM EGTA, 2 mM DTT), then incubated with streptavidin (1 mg/mL, New England Biolabs). The chamber was again washed with TIRF buffer, then incubated with 10 µL of a fresh dilution of microtubules (2 µL of microtubules diluted into 10 µL TIRF-Casein buffer (TIRF buffer supplemented with 50 mM KCl and 1 mg/mL casein) for 1 min. Chambers were then blocked with 50 µL TIRF-Casein buffer.

Complexes were prepared by mixing each component at the following concentrations: TMR-dynein at 0.3 µM, dynactin at 0.4 µM, $JIP3_{1-185}$ at 16 µM, Lis1 at 50 µM. GF150 buffer was added to a final volume of 6 µL. Complexes were incubated on ice for 15 minutes then diluted with TIRF-Casein buffer to a final volume of 15 µL. 4 µL of complex were added to 16 µL of TIRF-Casein buffer supplemented with an oxygen scavenging system (0.2 mg/mL catalase, Merck; 1.5 mg/mL glucose oxidase, Merck; 0.45% (w/v) glucose) 1% BME, 5 mM Mg.ATP. This mix was flowed into the chamber. The sample was imaged immediately at 23°C using a TIRF microscope (Nikon Eclipse Ti inverted microscope equipped with a Nikon 100x TIRF oil immersion objective). For each sample, a microtubule image was acquired using a 488 nm laser. Following this a 500-frame movie was acquired (200 ms exposure, 4.1 fps) using a 561 nm laser. To analyse the data, ImageJ was used to generate kymographs from the tiff movie stacks. Events of similar length were picked to analyse velocity, run length and number of processive events/µm microtubule/min, using criteria outlined previously (Schlager et al. 2014, Urnavicius et al. 2018). Velocity was calculated using pixel size of 105 nm and frame rate of 236 ms/frame. Three replicates were performed for each sample, with velocities and number of processive events plotted using GraphPad Prism 7. Statistical significance was determined using ANOVA with Tukey's multiple comparison.

CryoEM sample preparation

The sample was prepared in a similar manner as described previously (Chaaban and Carter 2022). To polymerize microtubules, tubulin was diluted in microtubule buffer (25mM MES pH 6.5, 70mM NaCl, 1mM MgCl2, 1mM EGTA, 1mM DTT) with 6 mM GTP (MilliporeSigma) such that the final concentration of tubulin was 5 mg/mL (45 µM) tubulin and GTP was 3 mM. The mixture was incubated on ice for 5 min, and microtubules were polymerized at 37°C for ~1.5 hours. To stabilize the microtubules, polymerization buffer was supplemented with 20 µM paclitaxel. The microtubules were pelleted on a benchtop centrifuge (Eppendorf) at 20,000 rcf for 8 min at room temperature. The supernatant was discarded

and the pellet was resuspended in polymerization buffer with paclitaxel by pipetting up and down with a cut tip. The microtubules were pelleted and resuspended again using an uncut tip. The concentration was estimated using Bradford reagent (Biorad) and diluted to ~0.65 mg/mL (~6 µM). To assemble the dynein-dynactin-JIP3 complex in the presence of LIS1, the purified proteins were mixed in a 1:2:60:32 molar ratio (0.33 mg/mL dynein, 0.56 mg/mL dynactin, 0.8 mg/mL JIP3 and 0.8 mg/mL LIS1) in GF150 buffer supplemented with 1 mM DTT in a total volume of 10 µL and incubated on ice for 30 min. To bind the complex to microtubules, 9 µL complex was mixed at room temperature with 5 µL microtubules and 9 µL binding buffer A (77 mM HEPES pH 7.2, 51 mM KCl, 13 mM MgSO4, 2.6 mM EGTA, 2.6 mM DTT, 7.68 mM AMPPNP, 13 µM paclitaxel) such that the final concentrations of KCl and AMPPNP were 100 mM and 3 mM, respectively. After 15 min, the complex-bound microtubules were pelleted at 20,000 rcf for 8 min at room temperature. The pellet was resuspended in binding buffer B (30 mM HEPES pH 7.2, 50 mM KCl, 5 mM MgSO4, 1 mM EGTA, 1 mM DTT, 3 mM AMPPNP, 5 µM paclitaxel, and 0.01% IGEPAL (MilliporeSigma) using an uncut tip. 3.5 µL was applied to freshly glow discharged Quantifoil R2/2 300-square-mesh gold grids (Quantifoil) in a Vitrobot IV (ThermoFisher) at 100% humidity and 20°C, incubated for 30 s, and blotted for 0.5-2 s before being plunged into liquid ethane.

Cryo-EM data collection and image processing

The samples were imaged using a FEI Titan Krios (300 kV) equipped with a K3 detector and energy filter (20 eV slit size) (Gatan) using automated data collection (ThermoFisher EPU). A total of 20,339 movies were acquired at 81,000 X magnification (1.09 Å/pixel, 100 µm objective aperture, ~2.2 sec exposure, 54 frames, fluence was ~54 $e^-/Å^2$, -1.2 to -3 µm defocus range).

Global motion correction and dose-weighting were performed in Relion 4 using MotionCorr2 (Zheng et al. 2017) with a B-factor of 150 and 5X5 patches. The power spectrum of aligned frames were used for CTF estimation by CTFFIND4 (Rohou and Grigorieff 2015). Microtubules were picked from the micrographs using the single particle picking mode in crYOLO (Wagner et al. 2019) with a model that was trained on manually picked micrographs (~100) in filament mode. The output coordinates along each microtubule were spaced by 81 Å. The coordinates were then resampled to a 4nm interval using the multi-curve fitting script described previously (Chai et al. 2022) (https://github.com/PengxinChai). The coordinates for each microtubule were then further split into segments of 10-17 coordinates as this gave better results with the following microtubule subtraction step. Finally, microtubule subtraction was performed as described previously (Chai et al. 2022). The subtracted microtubules were then used to pick dynein-dynactin-JIP3 complexes using crYOLO. The 306,823 picked particles were imported into Cryosparc (Punjani et al. 2017) followed by 2D classification. The particles in classes showing dynein-dynactin were used for ab-initio initial model generation. Three initial models were generated which were then used for a round of heterogeneous refinement using all particles. A total of 105,522 particles belonging to the 3D class which displayed good density for dynein-dynactin were selected and imported into Relion4. The processing after this stage is similar to that performed in (Chaaban and Carter 2022). The particles were extracted with a box size of 200 pixels (4.36 Å/pix) and used for 3D refinement. A soft-edge mask was generated based on the resulting density and a subsequent 3D refinement was performed with the mask after re-extracting the particles with a box size of 800 pixels (1.09 Å/pix). The particles were then polished and used for a round of local refinement using a mask around dynein tails-dynactin-JIP3 resulting in a consensus structure at 4.50 Å resolution. The dynactin pointed end, dynactin barbed end and dynein-tail-JIP3 regions were masked for signal subtraction. Local refinement, defocus and astigmatism refinement, and 3D classification without alignment were performed to improve the resolution. The final maps were B-factor sharpened in Relion4. All masks, particle numbers, resolutions, classification parameters can be found in Figure S1.

Model building and refinement

The cryoEM model PDB-7Z8F (Chaaban and Carter 2022) was used as the initial model for dynein and dynactin. $JIP3_{1-185}$ and dynein LIC helix (DLIC) (427-439) bound to the JIP3 RH1 domain were predicted by AlphaFold (see next section). The models were docked into the composite cryoEM map as a rigid body using UCSF Chimera (Pettersen et al. 2004). The model then underwent several rounds of manual modelling in COOT (Emsley et al. 2010)and refinement was done in PHENIX (Afonine et al. 2018).

AlphaFold prediction

All structure predictions were performed using AlphaFold through a local installation of Colabfold 1.2.0 (Mirdita et al. 2022), running MMseqs2 (Mirdita et al. 2019) for homology searches and AlphaFold2 (Jumper et al. 2021) or AlphaFold2-Multimer (Evans et al. 2022) for the predictions of single or multiple chains, respectively. $JIP3_{1-185}$ was predicted by running Colabfold 1.2.0 on two copies of JIP3 1-185 (Q9UPT6). The RH domain-DLIC interaction was predicted by running Colabfold 1.2.0 on two copies each of the JIP3 1-99 (Q9UPT6) and two copies of DLIC 427-439 (O43237). The predicted aligned error (PAE) with respect to Phe433 of DLIC was mapped onto the predicted structure using PointPAE 1.0 (https://github.com/sami-chaaban/PointPAE) (doi: 10.5281/zenodo.6792801) and ChimeraX was used for visualization. The JIP3 HBS1 interaction with dynein was predicted by running Colabfold 1.2.0 on two copies of JIP3 73-180 (Q9UPT6), one copy of dynein heavy chain 576-864 (Q14204), and one copy of dynein intermediate chain 226-583 (Q13409). The PAE relative to JIP3 Gln93 was mapped onto the prediction as above for the RH1 domain-DLIC interaction.

References:

Afonine, P. V., B. K. Poon, R. J. Read, O. V. Sobolev, T. C. Terwilliger, A. Urzhumtsev and P. D. Adams (2018). "Real-space refinement in PHENIX for cryo-EM and crystallography." Acta Crystallogr D Struct Biol **74**(Pt 6): 531-544.

Arimoto, M., S. P. Koushika, B. C. Choudhary, C. Li, K. Matsumoto and N. Hisamoto (2011). "The Caenorhabditis elegans JIP3 protein UNC-16 functions as an adaptor to link kinesin-1 with cytoplasmic dynein." J Neurosci **31**(6): 2216-2224.

Baumbach, J., A. Murthy, M. A. McClintock, C. I. Dix, R. Zalyte, H. T. Hoang and S. L. Bullock (2017). "Lissencephaly-1 is a context-dependent regulator of the human dynein complex." Elife **6**.

Bowman, A. B., A. Kamal, B. W. Ritchings, A. V. Philp, M. McGrail, J. G. Gindhart and L. S. Goldstein (2000). "Kinesin-dependent axonal transport is mediated by the sunday driver (SYD) protein." Cell **103**(4): 583-594.

Byrd, D. T., M. Kawasaki, M. Walcoff, N. Hisamoto, K. Matsumoto and Y. Jin (2001). "UNC-16, a JNK-signaling scaffold protein, regulates vesicle transport in C. elegans." Neuron **32**(5): 787-800.

Canty, J. T., A. Hensley and A. Yildiz (2022). "TRAK adaptors coordinate the recruitment and activation of dynein and kinesin to control mitochondrial transport." bioRxiv: 10.1101/2021.1107.1130.454553.

Cason, S. E., P. J. Carman, C. Van Duyne, J. Goldsmith, R. Dominguez and E. L. F. Holzbaur (2021). "Sequential dynein effectors regulate axonal autophagosome motility in a maturation-dependent pathway." J Cell Biol **220**(7).

Cavalli, V., P. Kujala, J. Klumperman and L. S. Goldstein (2005). "Sunday Driver links axonal transport to damage signaling." J Cell Biol **168**(5): 775-787.

Celestino, R., J. B. Gama, A. F. Castro-Rodrigues, D. J. Barbosa, H. Rocha, E. A. d'Amico, A. Musacchio, A. X. Carvalho, J. H. Morais-Cabral and R. Gassmann (2022). "JIP3 interacts with dynein and kinesin-1 to regulate bidirectional organelle transport." J Cell Biol **221**(8): e202110057.

Chaaban, S. and A. P. Carter (2022). "Structure of dynein-dynactin on microtubules shows tandem recruitment of cargo adaptors." bioRxiv: 10.1101/2022.1103.1117.482250.

Chai, P., Q. Rao and K. Zhang (2022). "Multi-curve fitting and tubulin-lattice signal removal for structure determination of large microtubule-based

motors." bioRxiv: 10.1101/2022.1101.1122.477366.

Cockburn, J. J. B., S. J. Hesketh, P. Mulhair, M. Thomsen, M. J. O'Connell and M. Way (2018). "Insights into Kinesin-1 Activation from the Crystal Structure of KLC2 Bound to JIP3." Structure **26**(11): 1486-1498 e1486.

d'Amico, E., M. Ahmad, V. Cmentowski, M. Girbig, F. Müller, S. Wohlgemuth, A. Brockmeyer, S. Maffini, P. Janning, I. R. Vetter, A. P. Carter, A. Perrakis and A. Musacchio (2022). "Conformational transitions of the mitotic adaptor Spindly underlie its interaction with Dynein and Dynactin." bioRxiv: 10.1101/2022.1102.1102.478874.

Drerup, C. M. and A. V. Nechiporuk (2013). "JNK-interacting protein 3 mediates the retrograde transport of activated c-Jun N-terminal kinase and lysosomes." PLoS Genet **9**(2): e1003303.

Edwards, S. L., S. C. Yu, C. M. Hoover, B. C. Phillips, J. E. Richmond and K. G. Miller (2013). "An organelle gatekeeper function for Caenorhabditis elegans UNC-16 (JIP3) at the axon initial segment." Genetics **194**(1): 143-161.

Elshenawy, M. M., E. Kusakci, S. Volz, J. Baumbach, S. L. Bullock and A. Yildiz (2020). "Lis1 activates dynein motility by modulating its pairing with dynactin." Nat Cell Biol **22**(5): 570-578.

Emsley, P., B. Lohkamp, W. G. Scott and K. Cowtan (2010). "Features and development of Coot." Acta Crystallogr D Biol Crystallogr **66**(Pt 4): 486-501.

Evans, R., M. O'Neill, A. Pritzel, N. Antropova, A. Senior, T. Green, A. Žídek, R. Bates, S. Blackwell, J. Yim, O. Ronneberger, S. Bodenstein, M. Zielinski, A. Bridgland, A. Potapenko, A. Cowie, K. Tunyasuvunakool, R. Jain, E. Clancy, P. Kohli, J. Jumper and D. Hassabis (2022). "Protein complex prediction with AlphaFold-Multimer." bioRxiv: 10.1101/2021.1110.1104.463034.

Fenton, A. R., T. A. Jongens and E. L. F. Holzbaur (2021). "Mitochondrial adaptor TRAK2 activates and functionally links opposing kinesin and dynein motors." Nat Commun **12**(1): 4578.

Gama, J. B., C. Pereira, P. A. Simoes, R. Celestino, R. M. Reis, D. J. Barbosa, H. R. Pires, C. Carvalho, J. Amorim, A. X. Carvalho, D. K. Cheerambathur and R. Gassmann (2017). "Molecular mechanism of dynein recruitment to kinetochores by the Rod-Zw10-Zwilch complex and Spindly." J Cell Biol **216**(4): 943-960.

Garner, K. E. L., A. Salter, C. Lau, M. Gurusaran, C. Villemant, E. P. Granger, G. McNee, P. G. Woodman, O. R. Davies, B. E. Burke and V. J. Allan (2022). "The meiotic LINC complex component KASH5 is an activating adaptor for cytoplasmic dynein." bioRxiv: 10.1101/2022.1104.1113.488131.

Gowrishankar, S., L. Lyons, N. M. Rafiq, A. Roczniak-Ferguson, P. De Camilli and S. M. Ferguson (2021). "Overlapping roles of JIP3 and JIP4 in promoting axonal transport of lysosomes in human iPSC-derived neurons." Mol Biol Cell **32**(11): 1094-1103.

Gowrishankar, S., Y. Wu and S. M. Ferguson (2017). "Impaired JIP3-dependent axonal lysosome transport promotes amyloid plaque pathology." J Cell Biol **216**(10): 3291-3305.

Guedes-Dias, P. and E. L. F. Holzbaur (2019). "Axonal transport: Driving synaptic function." Science **366**(6462).

Hammond, J. W., K. Griffin, G. T. Jih, J. Stuckey and K. J. Verhey (2008). "Co-operative versus independent transport of different cargoes by Kinesin-1." Traffic **9**(5): 725-741.

Hoogenraad, C. C., P. Wulf, N. Schiefermeier, T. Stepanova, N. Galjart, J. V. Small, F. Grosveld, C. I. de Zeeuw and A. Akhmanova (2003). "Bicaudal D induces selective dynein-mediated microtubule minus end-directed transport." EMBO J **22**(22): 6004-6015.

Htet, Z. M., J. P. Gillies, R. W. Baker, A. E. Leschziner, M. E. DeSantis and S. L. Reck-Peterson (2020). "LIS1 promotes the formation of activated cytoplasmic dynein-1 complexes." Nat Cell Biol **22**(5): 518-525.

Huang, S. H., S. Duan, T. Sun, J. Wang, L. Zhao, Z. Geng, J. Yan, H. J. Sun and Z. Y. Chen (2011). "JIP3 mediates TrkB axonal anterograde transport and enhances BDNF signaling by directly bridging TrkB with kinesin-1." J Neurosci **31**(29): 10602-10614.

Ito, M., K. Yoshioka, M. Akechi, S. Yamashita, N. Takamatsu, K. Sugiyama, M. Hibi, Y. Nakabeppu, T. Shiba and K. I. Yamamoto (1999). "JSAP1, a novel jun N-terminal protein kinase (JNK)-binding protein that functions as a Scaffold factor in the JNK

signaling pathway." Mol Cell Biol **19**(11): 7539-7548.

Jordens, I., M. Fernandez-Borja, M. Marsman, S. Dusseljee, L. Janssen, J. Calafat, H. Janssen, R. Wubbolts and J. Neefjes (2001). "The Rab7 effector protein RILP controls lysosomal transport by inducing the recruitment of dynein-dynactin motors." Curr Biol **11**(21): 1680-1685.

Jumper, J., R. Evans, A. Pritzel, T. Green, M. Figurnov, O. Ronneberger, K. Tunyasuvunakool, R. Bates, A. Zidek, A. Potapenko, A. Bridgland, C. Meyer, S. A. A. Kohl, A. J. Ballard, A. Cowie, B. Romera-Paredes, S. Nikolov, R. Jain, J. Adler, T. Back, S. Petersen, D. Reiman, E. Clancy, M. Zielinski, M. Steinegger, M. Pacholska, T. Berghammer, S. Bodenstein, D. Silver, O. Vinyals, A. W. Senior, K. Kavukcuoglu, P. Kohli and D. Hassabis (2021). "Highly accurate protein structure prediction with AlphaFold." Nature **596**(7873): 583-589.

Kelkar, N., S. Gupta, M. Dickens and R. J. Davis (2000). "Interaction of a mitogen-activated protein kinase signaling module with the neuronal protein JIP3." Mol Cell Biol **20**(3): 1030-1043.

Kendrick, A. A., A. M. Dickey, W. B. Redwine, P. T. Tran, L. P. Vaites, M. Dzieciatkowska, J. W. Harper and S. L. Reck-Peterson (2019). "Hook3 is a scaffold for the opposite-polarity microtubule-based motors cytoplasmic dynein-1 and KIF1C." J Cell Biol **218**(9): 2982-3001.

Keren-Kaplan, T., A. Saric, S. Ghosh, C. D. Williamson, R. Jia, Y. Li and J. S. Bonifacino (2022). "RUFY3 and RUFY4 are ARL8 effectors that promote coupling of endolysosomes to dynein-dynactin." Nat Commun **13**(1): 1506.

Kumar, G., P. Chawla, N. Dhiman, S. Chadha, S. Sharma, K. Sethi, M. Sharma and A. Tuli (2022). "RUFY3 links Arl8b and JIP4-Dynein complex to regulate lysosome size and positioning." Nat Commun **13**(1): 1540.

Lau, C. K., F. J. O'Reilly, B. Santhanam, S. E. Lacey, J. Rappsilber and A. P. Carter (2021). "Cryo-EM reveals the complex architecture of dynactin's shoulder region and pointed end." EMBO J **40**(8): e106164.

Lee, I. G., S. E. Cason, S. S. Alqassim, E. L. F. Holzbaur and R. Dominguez (2020). "A tunable LIC1-adaptor interaction modulates dynein activity in a cargo-specific manner." Nat Commun **11**(1): 5695.

Lee, I. G., M. A. Olenick, M. Boczkowska, C. Franzini-Armstrong, E. L. F. Holzbaur and R. Dominguez (2018). "A conserved interaction of the dynein light intermediate chain with dynein-dynactin effectors necessary for processivity." Nat Commun **9**(1): 986.

Lise, M. F., D. P. Srivastava, P. Arstikaitis, R. L. Lett, R. Sheta, V. Viswanathan, P. Penzes, T. P. O'Connor and A. El-Husseini (2009). "Myosin-Va-interacting protein, RILPL2, controls cell shape and neuronal morphogenesis via Rac signaling." J Cell Sci **122**(Pt 20): 3810-3821.

McKenney, R. J., W. Huynh, M. E. Tanenbaum, G. Bhabha and R. D. Vale (2014). "Activation of cytoplasmic dynein motility by dynactin-cargo adapter complexes." Science **345**(6194): 337-341.

Mirdita, M., K. Schutze, Y. Moriwaki, L. Heo, S. Ovchinnikov and M. Steinegger (2022). "ColabFold: making protein folding accessible to all." Nat Methods **19**(6): 679-682.

Mirdita, M., M. Steinegger and J. Soding (2019). "MMseqs2 desktop and local web server app for fast, interactive sequence searches." Bioinformatics **35**(16): 2856-2858.

Montagnac, G., J. B. Sibarita, S. Loubery, L. Daviet, M. Romao, G. Raposo and P. Chavrier (2009). "ARF6 Interacts with JIP4 to control a motor switch mechanism regulating endosome traffic in cytokinesis." Curr Biol **19**(3): 184-195.

Nguyen, Q., C. M. Lee, A. Le and E. P. Reddy (2005). "JLP associates with kinesin light chain 1 through a novel leucine zipper-like domain." J Biol Chem **280**(34): 30185-30191.

Pettersen, E. F., T. D. Goddard, C. C. Huang, G. S. Couch, D. M. Greenblatt, E. C. Meng and T. E. Ferrin (2004). "UCSF Chimera--a visualization system for exploratory research and analysis." J Comput Chem **25**(13): 1605-1612.

Punjani, A., J. L. Rubinstein, D. J. Fleet and M. A. Brubaker (2017). "cryoSPARC: algorithms for rapid unsupervised cryo-EM structure determination." Nat Methods **14**(3): 290-296.

Reck-Peterson, S. L., W. B. Redwine, R. D. Vale and A. P. Carter (2018). "The cytoplasmic dynein transport machinery and its many cargoes." Nat Rev Mol Cell Biol **19**(6): 382-398.

Rohou, A. and N. Grigorieff (2015). "CTFFIND4: Fast and accurate defocus estimation from electron micrographs." J Struct Biol **192**(2): 216-221.

Sacristan, C., M. U. D. Ahmad, J. Keller, J. Fermie, V. Groenewold, E. Tromer, A. Fish, R. Melero, J. M. Carazo, J. Klumperman, A. Musacchio, A. Perrakis and G. J. Kops (2018). "Dynamic kinetochore size regulation promotes microtubule capture and chromosome biorientation in mitosis." Nat Cell Biol **20**(7): 800-810.

Schlager, M. A., H. T. Hoang, L. Urnavicius, S. L. Bullock and A. P. Carter (2014). "In vitro reconstitution of a highly processive recombinant human dynein complex." EMBO J **33**(17): 1855-1868.

Schroeder, C. M., J. M. Ostrem, N. T. Hertz and R. D. Vale (2014). "A Ras-like domain in the light intermediate chain bridges the dynein motor to a cargo-binding region." Elife **3**: e03351.

Schroeder, C. M. and R. D. Vale (2016). "Assembly and activation of dynein-dynactin by the cargo adaptor protein Hook3." J Cell Biol **214**(3): 309-318.

Siddiqui, N., A. J. Zwetsloot, A. Bachmann, D. Roth, H. Hussain, J. Brandt, I. Kaverina and A. Straube (2019). "PTPN21 and Hook3 relieve KIF1C autoinhibition and activate intracellular transport." Nat Commun **10**(1): 2693.

Sun, F., C. Zhu, R. Dixit and V. Cavalli (2011). "Sunday Driver/JIP3 binds kinesin heavy chain directly and enhances its motility." EMBO J **30**(16): 3416-3429.

Urnavicius, L., C. K. Lau, M. M. Elshenawy, E. Morales-Rios, C. Motz, A. Yildiz and A. P. Carter (2018). "Cryo-EM shows how dynactin recruits two dyneins for faster movement." Nature **554**(7691): 202-206.

Urnavicius, L., K. Zhang, A. G. Diamant, C. Motz, M. A. Schlager, M. Yu, N. A. Patel, C. V. Robinson and A. P. Carter (2015). "The structure of the dynactin complex and its interaction with dynein." Science **347**(6229): 1441-1446.

Verhey, K. J., D. Meyer, R. Deehan, J. Blenis, B. J. Schnapp, T. A. Rapoport and B. Margolis (2001). "Cargo of kinesin identified as JIP scaffolding proteins and associated signaling molecules." J Cell Biol **152**(5): 959-970.

Vilela, F., C. Velours, M. Chenon, M. Aumont-Nicaise, V. Campanacci, A. Thureau, O. Pylypenko, J. Andreani, P. Llinas and J. Menetrey (2019). "Structural characterization of the RH1-LZI tandem of JIP3/4 highlights RH1 domains as a cytoskeletal motor-binding motif." Sci Rep **9**(1): 16036.

Wagner, T., F. Merino, M. Stabrin, T. Moriya, C. Antoni, A. Apelbaum, P. Hagel, O. Sitsel, T. Raisch, D. Prumbaum, D. Quentin, D. Roderer, S. Tacke, B. Siebolds, E. Schubert, T. R. Shaikh, P. Lill, C. Gatsogiannis and S. Raunser (2019). "SPHIRE-crYOLO is a fast and accurate fully automated particle picker for cryo-EM." Commun Biol **2**: 218.

Wang, T., K. K. Wong and W. Hong (2004). "A unique region of RILP distinguishes it from its related proteins in its regulation of lysosomal morphology and interaction with Rab7 and Rab34." Mol Biol Cell **15**(2): 815-826.

Watt, D., R. Dixit and V. Cavalli (2015). "JIP3 Activates Kinesin-1 Motility to Promote Axon Elongation." J Biol Chem **290**(25): 15512-15525.

Willett, R., J. A. Martina, J. P. Zewe, R. Wills, G. R. V. Hammond and R. Puertollano (2017). "TFEB regulates lysosomal positioning by modulating TMEM55B expression and JIP4 recruitment to lysosomes." Nat Commun **8**(1): 1580.

Wu, M., T. Wang, E. Loh, W. Hong and H. Song (2005). "Structural basis for recruitment of RILP by small GTPase Rab7." EMBO J **24**(8): 1491-1501.

Zheng, S. Q., E. Palovcak, J. P. Armache, K. A. Verba, Y. Cheng and D. A. Agard (2017). "MotionCor2: anisotropic correction of beam-induced motion for improved cryo-electron microscopy." Nat Methods **14**(4): 331-332.

Zivanov, J., T. Nakane, B. O. Forsberg, D. Kimanius, W. J. Hagen, E. Lindahl and S. H. Scheres (2018). "New tools for automated high-resolution cryo-EM structure determination in RELION-3." Elife **7**.

Supplementary figures

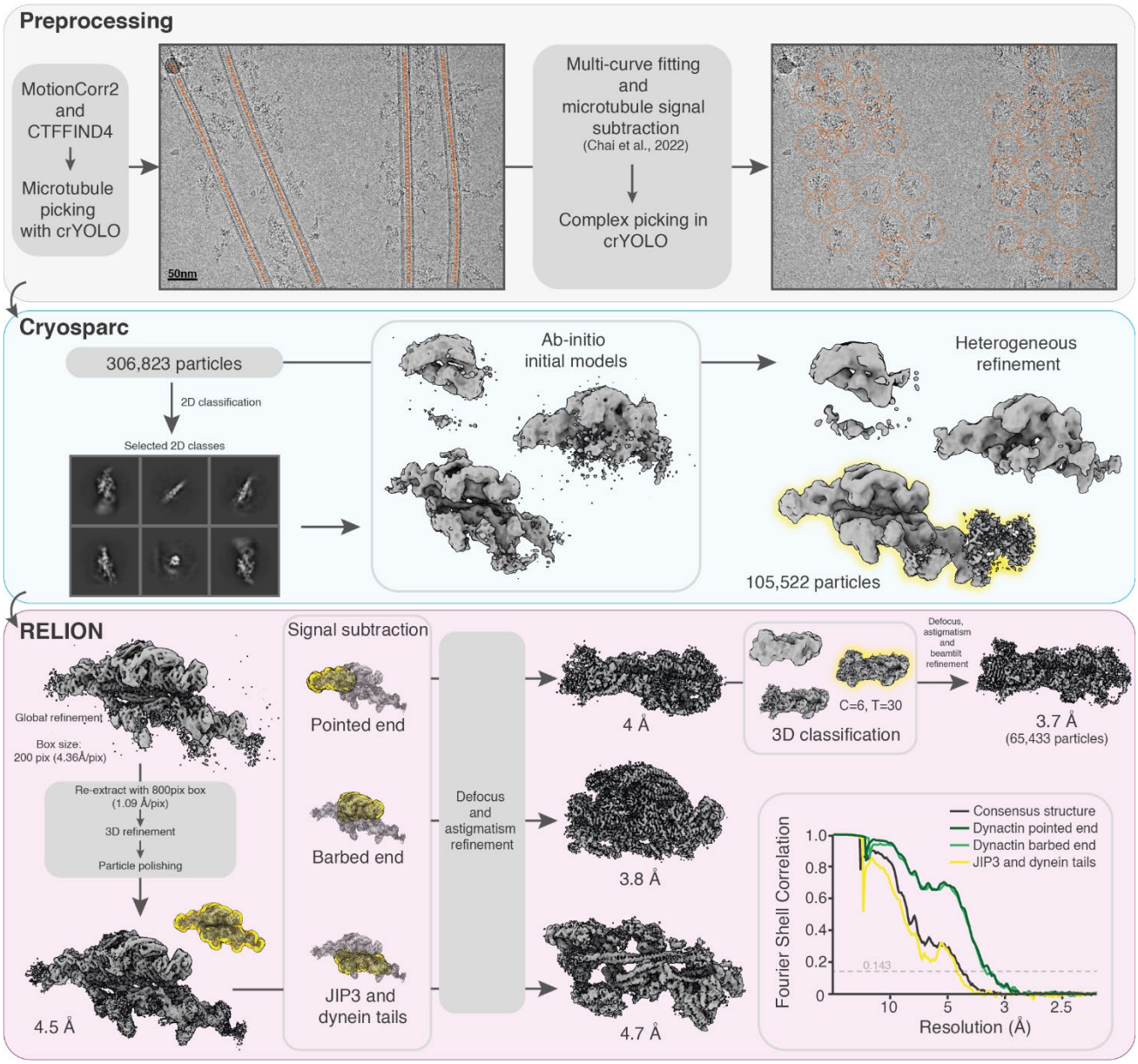

Figure S1. CryoEM image processing pipeline. The 3D class selected after heterogeneous refinement or 3D classification (performed without alignment) are represented with a yellow halo. T = tau fudge, C = number of classes. Masks used for 3D refinement and signal subtraction are shown in yellow. Plots show the gold standard Fourier Shell Correlation. The dotted horizontal line shows the 0.143 cutoff.

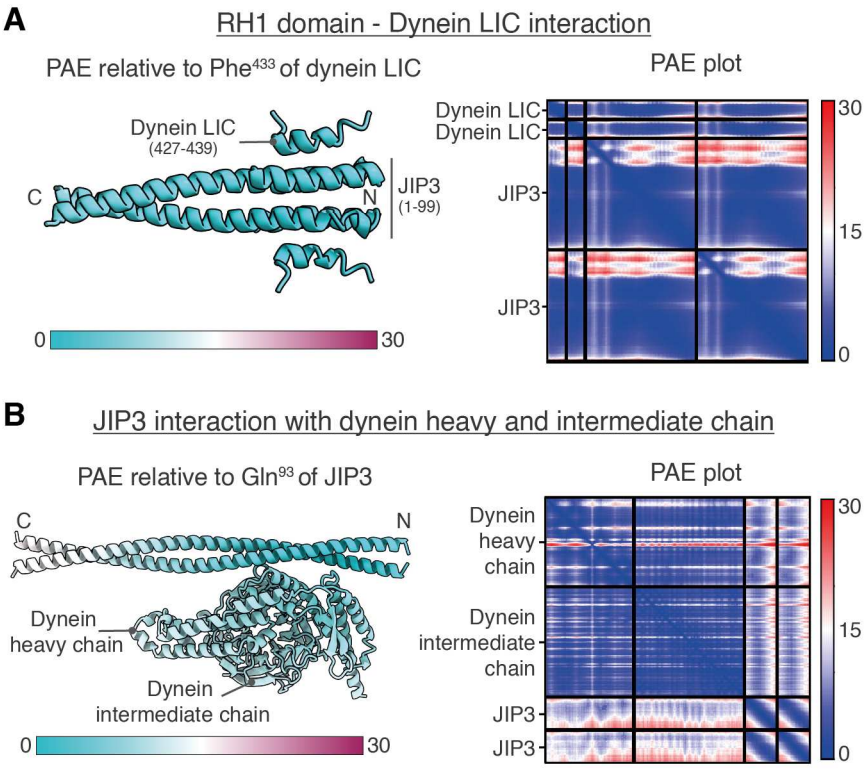

Figure S2. Alphafold predictions of protein interactions. Alpha fold prediction of **(A)** JIP3 RH1 domain along with two copies of DLIC helix (427-439) and **(B)** JIP3 HBS1 region along with two copies of dynein heavy chain (576-864), and dynein intermediate chain (226-583). Relative PAE plots are shown on the left where lower values represent higher confidence. The full PAE plot is shown on the right.